SCIENTIFIC REP🞿RTS

OPEN

Local structure, nucleation sites and crystallization behavior and their effects on magnetic properties of $Fe_{81}Si_xB_{10}P_{8-x}Cu_1$ ($x = 0$~8)

C. C. Cao[1], Y. G. Wang[1], L. Zhu[1], Y. Meng[1], X. B. Zhai[1], Y. D. Dai[1], J. K. Chen[1] & F. M. Pan[2]

In this work, an attempt has been made to reveal critical factors dominating the crystallization and soft magnetic properties of $Fe_{81}Si_xB_{10}P_{8-x}Cu_1$ ($x = 0$, 2, 4, 6 and 8) alloys. Both melt spun and annealed alloys are characterized by differential scanning calorimetry, X-ray diffractometry, Mössbauer spectroscopy, transmission electron microscopy, positron annihilation lifetime spectroscopy and magnetometry. The changes in magnetic interaction between Fe atoms and chemical homogeneity can well explain the variation of magnetic properties of $Fe_{81}Si_xB_{10}P_{8-x}Cu_1$ amorphous alloys. The density of nucleation sites in the amorphous precursors decreases in the substitution of P by Si. Meanwhile, the precipitated nanograins gradually coarsen, but the inhibiting effect of P on grain growth diminishes causing the increase of the crystallinity. Moreover, various site occupancies of Si are observed in the nanocrystallites and the Si occupancy in *bcc* Fe decreases the average magnetic moment of nanograins. Without sacrificing amorphous forming ability, we can obtain FeSiBPCu nanocrystalline alloy with excellent soft magnetic properties by optimizing the content of Si and P in the amorphous precursors.

Fe-based nanocrystalline soft magnetic alloys with the amorphous/crystalline composite structures have become a hot topic in both research and application. These alloys usually possess outstanding magnetic properties involving high saturation magnetic flux density (B_S) and low coercivity (H_C)[1–4]. Current state of the art nanocrystalline alloys mainly include FeSiBNbCu[5], FeSiBPCu[6], FeMBCu (M = Zr, Nb, Hf)[7] and their derivatives which contain a handful of early transition metal elements to promote their crystallization[8]. It is noteworthy that soft magnetic properties of these alloys are usually variable even if the atomic percent of magnetic Fe atoms keeps the same. For example, $Fe_{82.65}Cu_{1.35}Si_2B_{14}$ nanocrystalline alloy shows an H_C of 6.5 A/m and a B_S of 1.84 T, while the H_C and B_S of $Fe_{82.65}Cu_{1.35}Si_5B_{11}$ are 60 A/m and 1.81 T, respectively[9]. Magnetic properties of nanocrystalline alloys are closely associated with the amount, size and chemical composition of nanograins embedded in the amorphous matrix.

Every kind of metalloid and transition metal element plays an essential role on the nanocrystallization and only with appropriate content can the magnetic properties be improved. It has been proven that moderate addition of Cu can provide nucleation sites for α-Fe and thus refines the primary nanocrystallites due to the formation of Cu clusters[10,11]. Moreover, the differences in the kind and content of solute elements usually result in various structures and chemical compositions of nanograins. For instance, α-Fe phase with *bcc* structure precipitates out in the $Fe_{83.3}Si_4B_8P_4Cu_{0.7}$ alloy[12], but Fe_3Si phase with DO_3 structure precipitates out in the $Fe_{73.5}Si_{13.5}B_9Nb_3Cu_1$ alloy[13]. The composition of precipitated nanograins varies with the content of Si even in the same system, such as in FeSiBCu[14] and FeSiBNbCu alloys[15], respectively. In addition, the co-addition of Cu and P can further refine the nanograins, which results from the interaction between solute atoms forming CuP clusters[16]. The crystallization process tightly contacts with the microstructure of amorphous precursors including short range order, free volume, chemical homogeneity and particularly nucleation sites. Thus comprehensively understanding the transformation of amorphous precursors during the crystallization appears to be significantly important for advanced materials design.

For those nanocrystalline alloys with heterogeneous nucleation, various methods have been proposed to increase nucleation sites for the refinement of nanograins, such as the addition of Cu into the FeZrNbB alloy[17].

[1]College of Materials Science and Technology, Nanjing University of Aeronautics and Astronautics, Nanjing, 211106, P. R. China. [2]College of Science, Nanjing University of Aeronautics and Astronautics, Nanjing, 211106, P. R. China. Correspondence and requests for materials should be addressed to Y.G.W. (email: yingang.wang@nuaa.edu.cn)
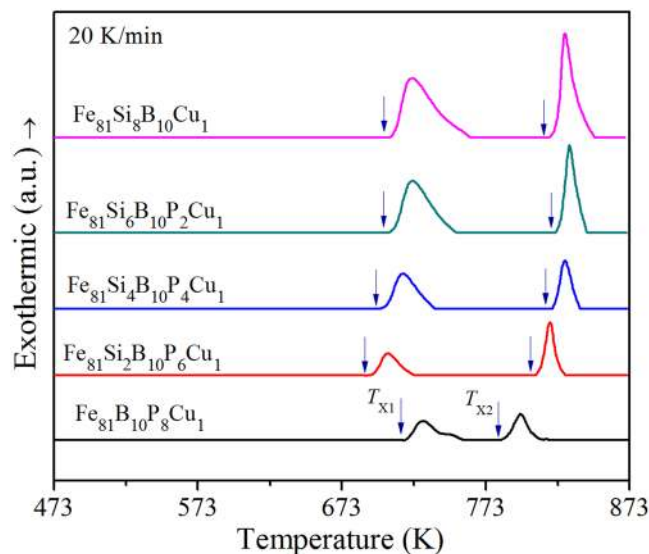
Figure 1. DSC curves of melt spun $Fe_{81}Si_xB_{10}P_{8-x}Cu_1$ ($x = 0\sim8$) ribbons.

When the amorphous precursors contain insoluble atoms or atom pairs, such as Cu, Nb and Cu-P, they tend to precipitate out and agglomerate to form insoluble clusters at the early stage of annealing process which can serve as nucleation sites for nanograins. However, little is known about the real content of nucleation sites during the crystallization which is usually reflected by the size of nanograins. It is probable to be inaccurate in some cases because some solute atoms such as P can also restrain the growth of nanograins[18]. The difficulty lies in the facts that nucleation sites are too small to be characterized and that one can hardly discern which clusters can effectively serve as nucleation sites. But from another point of view, crystallites precipitate out on nucleation sites at the very beginning of crystallization with the formation of nanovoids at grain boundaries[19]. Positron annihilation lifetime spectroscopy (PALS) is an efficient method to provide precise information about characteristic positron annihilation sites in nanocrystalline alloys, such as interstitial holes, vacancies and grain boundaries[20,21]. This technology can be used to characterize the formation and growth of crystallites, which can effectively reflect the density of nucleation sites during the crystallization. Meanwhile, Mössbauer spectroscopy can precisely identify the local structure around atomic nucleus for its high energy resolution, with which the information about short-range order in the amorphous matrix and chemical compositions of the nanograins can be obtained[22].

In this work, we analyze the local structure differences in both melt spun and annealed $Fe_{81}Si_xB_{10}P_{8-x}Cu_1$ ($x = 0, 2, 4, 6$ and 8) alloys to reveal the critical factors dominating the crystallization. Specifically, we focus on the microstructure of amorphous precursors, nucleation sites at the beginning of crystallization and crystal phases after the nanocrystallization. Furthermore, we are aiming at understanding the effects of local structure, nucleation sites and crystallization behavior of the amorphous precursors on magnetic properties of nanocrystalline alloys.

Results and Discussion

Thermal properties.   As shown in Fig. 1, differential scanning calorimetry (DSC) curves are collected to investigate the thermal dynamic characteristics of $Fe_{81}Si_xB_{10}P_{8-x}Cu_1$ ($x = 0, 2, 4, 6$ and 8) alloys. All these alloys have two conspicuous and separated exothermic peaks marked as T_{X1} and T_{X2}, which indicates that the crystallization of $Fe_{81}Si_xB_{10}P_{8-x}Cu_1$ alloys occurs in two stages. For $Fe_{81}Si_xB_{10}P_{8-x}Cu_1$ alloys with $x = 0, 2, 4, 6$ and 8, T_{X1} is 713, 688, 697, 701 and 704 K, respectively. It is worth noting that 2at. % of Si significantly advances the primary crystallization but postpones the secondary crystallization, and then both T_{X1} and T_{X2} increase gradually with Si further substituting for P. The temperature interval ($\Delta T_X = T_{X2} - T_{X1}$) between the two peaks shows a maximum of about 117 K for $Fe_{81}Si_4B_{10}P_4Cu_1$ alloy. The smaller ΔT_X means the more strict annealing treatment during the crystallization process, especially for $Fe_{81}B_{10}P_8Cu_1$ alloy in which the secondary crystallization practically tends to occur. Thus, appropriate Si superseding P in $Fe_{81}Si_xB_{10}P_{8-x}Cu_1$ alloys provides an advantage for the nanocrystallization.

Local structure in amorphous precursors and crystal phases.   Figure 2 shows the X-ray diffractometry (XRD) patterns for the melt spun and annealed $Fe_{81}Si_xB_{10}P_{8-x}Cu_1$ ($x = 0, 2, 4, 6$ and 8) alloys. Each diffraction pattern of the melt spun ribbons in Fig. 2(a) exhibiting a typical broad halo without any appreciable crystalline peak indicates the formation of amorphous structure. According to the results of DSC, all $Fe_{81}Si_xB_{10}P_{8-x}$ alloy ribbons are annealed at their individual T_{X1} for 5 min. As shown in Fig. 2(b), a weak crystalline peak located at $2\theta = 45°$ corresponding to *bcc* Fe suggests the beginning of primary crystallization. Figure 2(c) presents the diffraction patterns of the $Fe_{81}Si_xB_{10}P_{8-x}Cu_1$ nanocrystalline alloys obtained by annealing their amorphous precursors at 743 K for 5 minutes. In each pattern, there appear three distinct diffraction peaks corresponding to *bcc* Fe phase. The intensity of these peaks is enhanced as Si content x increases, which implies that the crystallinity of
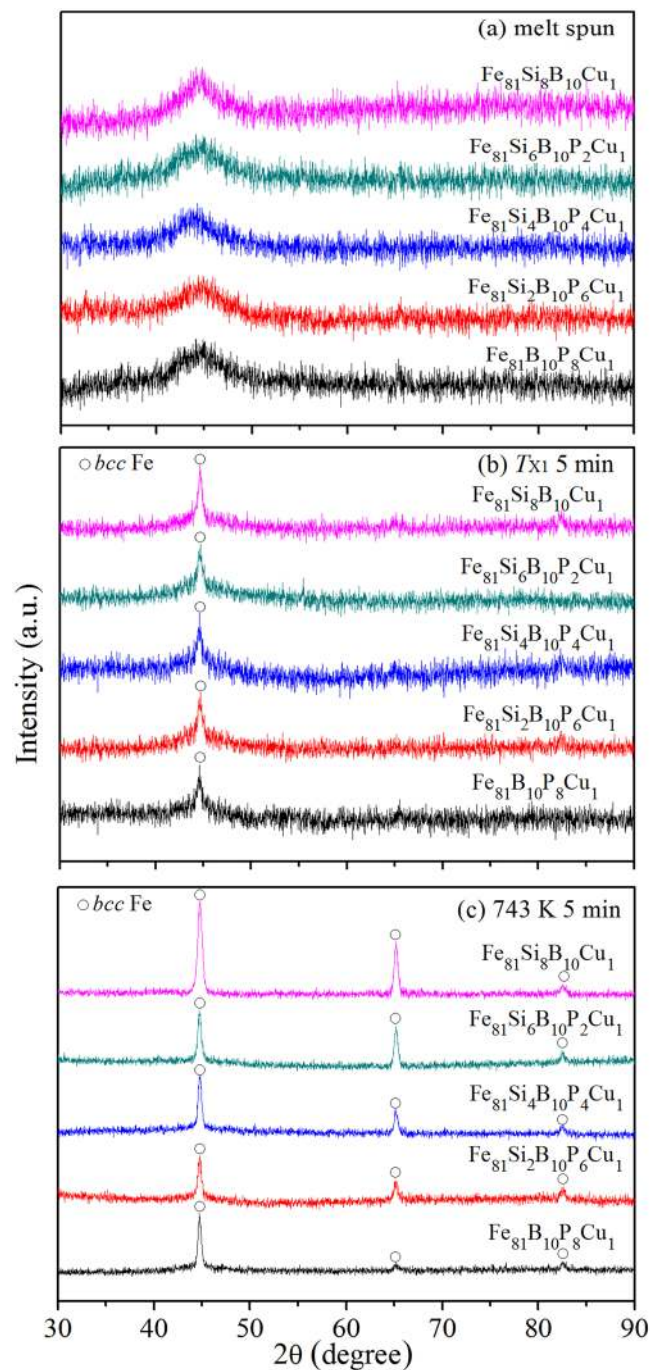
Figure 2. XRD patterns of $Fe_{81}Si_xB_{10}P_{8-x}Cu_1$ ($x = 0 \sim 8$) melt spun ribbons (**a**) and those annealed at T_{X1} (**b**) and 743 K (**c**) for 5 min.

$Fe_{81}Si_xB_{10}P_{8-x}Cu_1$ alloys increases with P gradually replaced by Si. Meanwhile, according to the Scherrer equation, the average mean grain size of the α-Fe phase is estimated to increase.

A further study with Mössbauer spectroscopy provides more detailed information about the microstructure of as-quenched and nanocrystalline $Fe_{81}Si_xB_{10}P_{8-x}Cu_1$ ($x = 0, 2, 4, 6$ and 8) alloys. As shown in Fig. 3(a), the wide and asymmetrical sextets demonstrate the amorphous nature of all the melt spun alloys[23]. The hyperfine parameters of fitted Mössbauer spectra are given in Table 1. Isomer shift (*IS*) refers to the observed shift of the resonance spectrum, quadrupole splitting (*QS*) results from the asymmetrical distribution of charge around atomic nucleus, and isomer shift change (*DTI*) is a coupling parameter that ensures the observed asymmetry of the experimental spectrum. The average magnetic hyperfine field ($B_{hf,a}$) is a parameter to describe the average hyperfine interaction and proportional to the spin-exchange interaction between magnetic atoms in each sample. It is noted that both $Fe_{81}B_{10}P_8Cu_1$ and $Fe_{81}Si_4B_{10}P_4Cu_1$ show relatively high $B_{hf,a}$ compared with the other amorphous alloys.
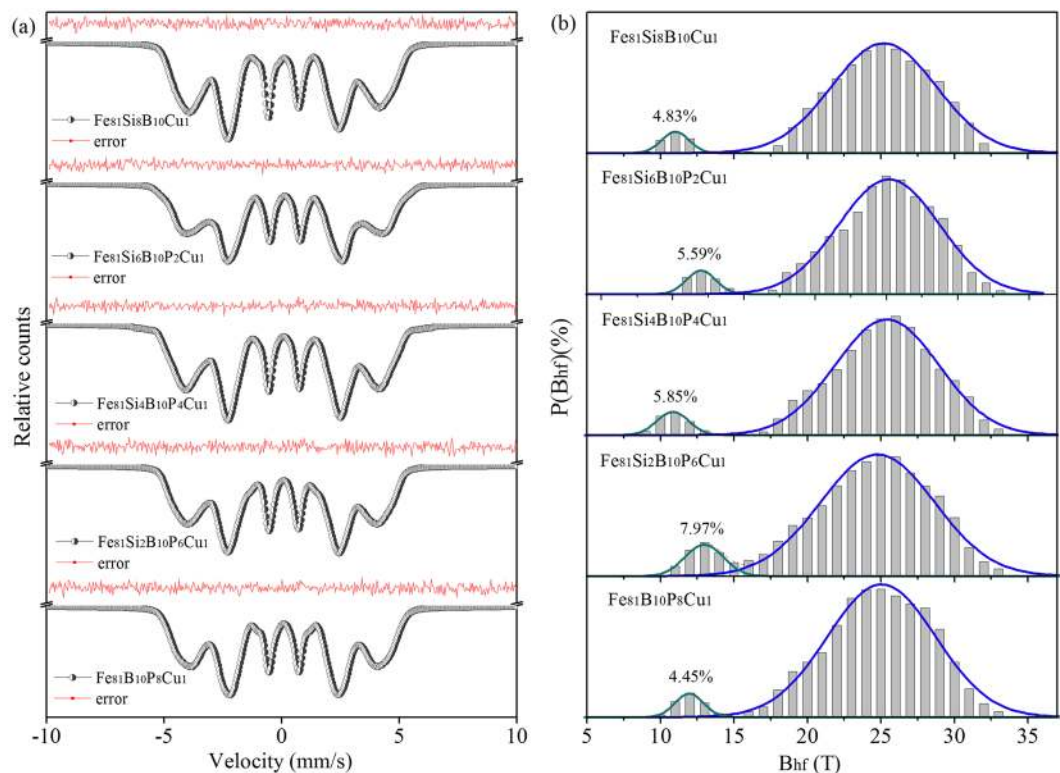
Figure 3. Mössbauer spectra (**a**) and corresponding hyperfine field distributions (**b**) of $Fe_{81}Si_xB_{10}P_{8-x}Cu_1$ ($x = 0 \sim 8$) melt spun ribbons.

Samples	IS (mm/s)	DTI (mm/s)	QS (mm/s)	$B_{hf,a}$ (T)
$Fe_{81}B_{10}P_8Cu_1$	0.104	0.0001	−0.0040	24.7
$Fe_{81}Si_2B_{10}P_6Cu_1$	0.043	0.0010	−0.0641	24.2
$Fe_{81}Si_4B_{10}P_4Cu_1$	0.096	0.0019	0.0032	24.5
$Fe_{81}S_6B_{10}P_2Cu_1$	0.027	0.0021	−0.0661	23.9
$Fe_{81}Si_8B_{10}Cu_1$	−0.079	0.0073	0.0361	23.7

Table 1. Hyperfine parameters of melt spun $Fe_{81}Si_xB_{10}P_{8-x}Cu_1$ ($x = 0 \sim 8$) ribbons: average magnetic hyperfine field ($B_{hf,a}$), change of isomer shift (*DTI*), Isomer shift relative to α-Fe (*IS*), quadrupole splitting (*QS*).

As reported early, the strengthened magnetic interaction can be ascribed to an increased degree of order in the topological structure[24].

Hyperfine field distributions obtained from the Mössbauer spectra of melt spun $Fe_{81}Si_xB_{10}P_{8-x}Cu_1$ alloys are depicted in Fig. 3(b). Magnetic hyperfine field distributions are usually decomposed into several components adopting Gaussian distributions to investigate the chemical short range orders in the structural relaxation or the crystal phases in the crystallization[25–27]. However, it is less accurate for melt spun metallic glasses where excess free volume and residual stress distort the coordination environment of Fe atoms. Nevertheless, all the hyperfine field distributions distinctly separate into two regions in Fig. 3(b) which suggests the coexistence of two distinguished zones in the amorphous structure of melt spun ribbons, namely the low field region (8 T to 15T) with weakened magnetic interactions and the high field region (15 T to 35 T) with enhanced magnetic interactions[28]. The low field region indicates Fe-deficient zones with plentiful B atoms and a little Cu atoms occupying in the neighbor shell of Fe atoms, while the high field region implies Fe enriched ones[29,30]. Therefore, the relative area of the low field region in Fig. 3(b) can be utilized to evaluate the chemical homogeneity of the amorphous structure. The maximum area ratio of the low field region in $Fe_{81}Si_2B_{10}P_6Cu_1$ alloy manifests a high degree of inhomogeneity in the amorphous structure which will promote the crystallization in the annealing, while the minimum value of that in $Fe_{81}B_{10}P_8Cu_1$ alloy leads to a high degree of homogeneity and a high T_{x1}, which is consistent with the results from DSC.

Figure 4 displays Mössbauer spectra and the corresponding hyperfine field distributions of $Fe_{81}Si_xB_{10}P_{8-x}Cu_1$ nanocrystalline alloys obtained by annealing their amorphous precursors at 743 K for 5 min. The split sextets superimposed upon the broadened spectra in Fig. 4(a) and the emergence of split peaks at about 33 T corresponding to *bcc* Fe in Fig. 4(b) characterize the microstructure with nanograins embedded in the residual
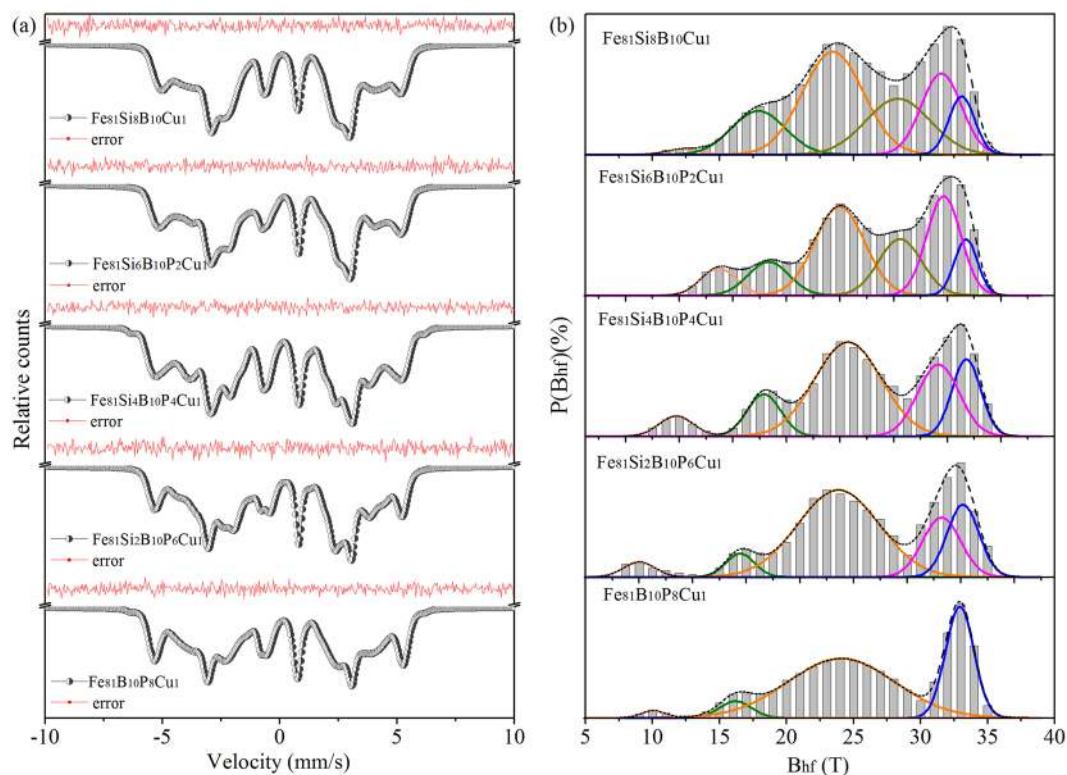
Figure 4. Mössbauer spectra (**a**) and corresponding hyperfine field distributions (**b**) of $Fe_{81}Si_xB_{10}P_{8-x}Cu_1$ ($x = 0\sim8$) nanocrystalline ribbons.

Samples	A8 (%)	A7 (%)	A6 (%)	*bcc* Fe (%)
$Fe_{81}B_{10}P_8Cu_1$	31.79			31.79
$Fe_{81}Si_2B_{10}P_6Cu_1$	18.02	17.71		35.73
$Fe_{81}Si_4B_{10}P_4Cu_1$	16.27	23.62		39.89
$Fe_{81}Si_6B_{10}P_2Cu_1$	9.30	24.43	17.53	51.26
$Fe_{81}Si_8B_{10}Cu_1$	7.78	21.92	23.48	53.18

Table 2. Area ratios of sub-peaks corresponding to A8, A7, A6 and *bcc* Fe in hyperfine field distributions of nanocrystalline $Fe_{81}Si_xB_{10}P_{8-x}Cu_1$ ($x = 0\sim 8$) ribbons.

amorphous matrix[31]. As reported previously[32], crystal phases in FeSi alloys (<10 at.% Si) prefer to form *bcc* Fe structure during the crystallization where the central Fe atom has 6~8 nearest-neighbor Fe atoms with Si atoms occupying at the residual sites. The *bcc* Fe structure with all the eight nearest sites occupied by Fe atoms is defined as an A8 configuration. Similarly, A7 and A6 configuration mean the *bcc* Fe structure with seven and six nearest-neighbor Fe atoms, respectively. Therefore, to further explore the specific site occupancy in the nanocrystallites of $Fe_{81}Si_xB_{10}P_{8-x}Cu_1$ alloys, the hyperfine field distributions are precisely decomposed into several components by Gaussian distributions. The gray histograms in Fig. 4(b) represent the actual hyperfine field distributions, while the dotted black lines represent the fitting results obtained from the corresponding colored components. The excellent match between them confirms that the Gaussian fitting results can provide accurate structural information of the FeSiBPCu nanocrystalline alloys. Peaks at hyperfine fields of about 33 T, 31.5 T and 28.5 T can be attributed to A8, A7 and A6 configurations, respectively, as suggested by previous studies[14,33]. The other peaks in Fig. 4(b) can be assigned to Fe atoms with various coordination surroundings in the residual amorphous matrix. It is noteworthy that only nanograins with A8 configuration precipitate out in the $Fe_{81}B_{10}P_8Cu_1$ alloy because of the lack of Si, but for the rest alloys containing Si, both A8 and A7 configurations appear in the crystal phases resulting in the broadening or splitting of peaks. When *x* reaches 6, all the three configurations coexist in the *bcc* Fe crystal phases. The area ratio of each sub-peak and the sum of those corresponding to *bcc* Fe are shown in Table 2. With P gradually replaced by Si in the $Fe_{81}Si_xB_{10}P_{8-x}Cu_1$ alloys, Si atoms tend to occupy more nearest sites of Fe atoms in *bcc* Fe structure, which results in the nanocrystallites diversified and the crystallinity of alloy ribbons increasing. It can be attributed to two aspects. On one hand, Si is preferentially spread into *bcc* nanocrystallites compared with amorphous matrix during the primary crystallization[14,32]. On the other hand, the decrease of P in the amorphous matrix weakens its inhibiting effect on grain growth[34].
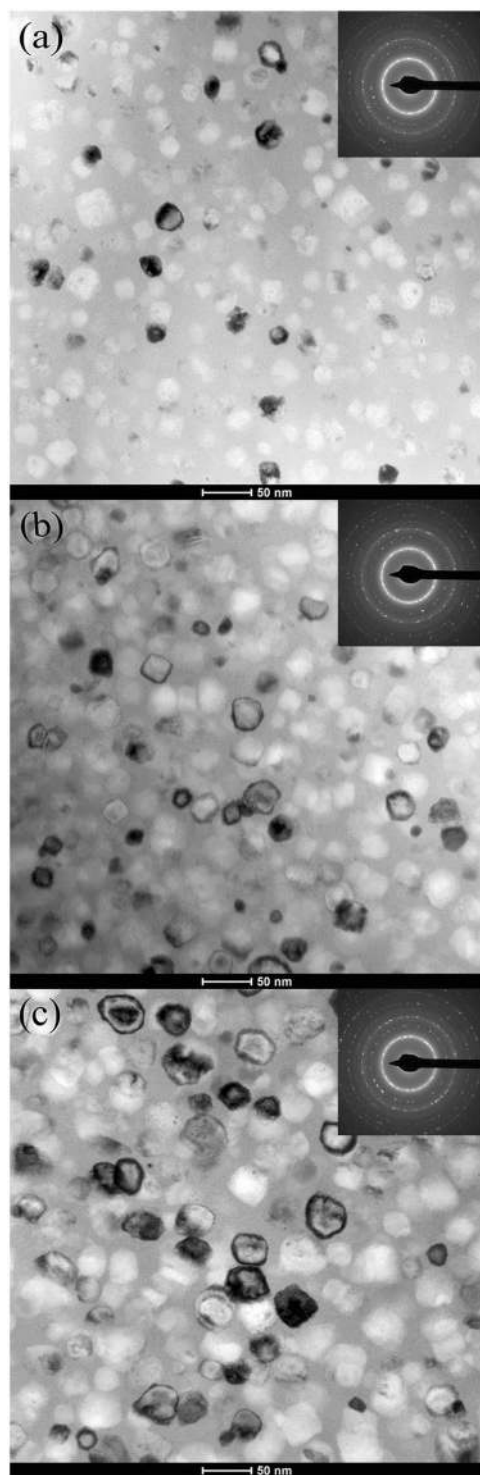
Figure 5. TEM bright field images and corresponding SAED patterns of (**a**) $Fe_{81}B_{10}P_8Cu_1$, (**b**) $Fe_{81}Si_4B_{10}P_4Cu_1$ and (**c**) $Fe_{81}Si_8B_{10}Cu_1$ ribbons annealed at 743 K for 5 min.

As shown in Fig. 5, the bright field images of transmission electron microscopy (TEM) and the corresponding selected area electron diffraction (SAED) patterns prove the amorphous/nanocrystalline composite structures of the 743 K annealed $Fe_{81}B_{10}P_8Cu_1$, $Fe_{81}Si_4B_{10}P_4Cu_1$ and $Fe_{81}Si_8B_{10}Cu_1$ ribbons, and the average grain sizes are 20 nm, 25 nm and 36 nm, respectively. It suggests that, accompanied with the crystallinity increasing, the nanograins coarsen with P replaced by Si, which agrees well with the XRD observation. It is reported that CuP clusters have the ability of reducing the atomic migration and pining down the growth of α-Fe[35]. Therefore, by replacing P with Si in the $Fe_{81}Si_xB_{10}P_{8-x}Cu_1$ alloys, except the inhibiting effect of P on grain growth diminishing, the density of CuP clusters may also decrease which is expected to cause the increase of grain size.
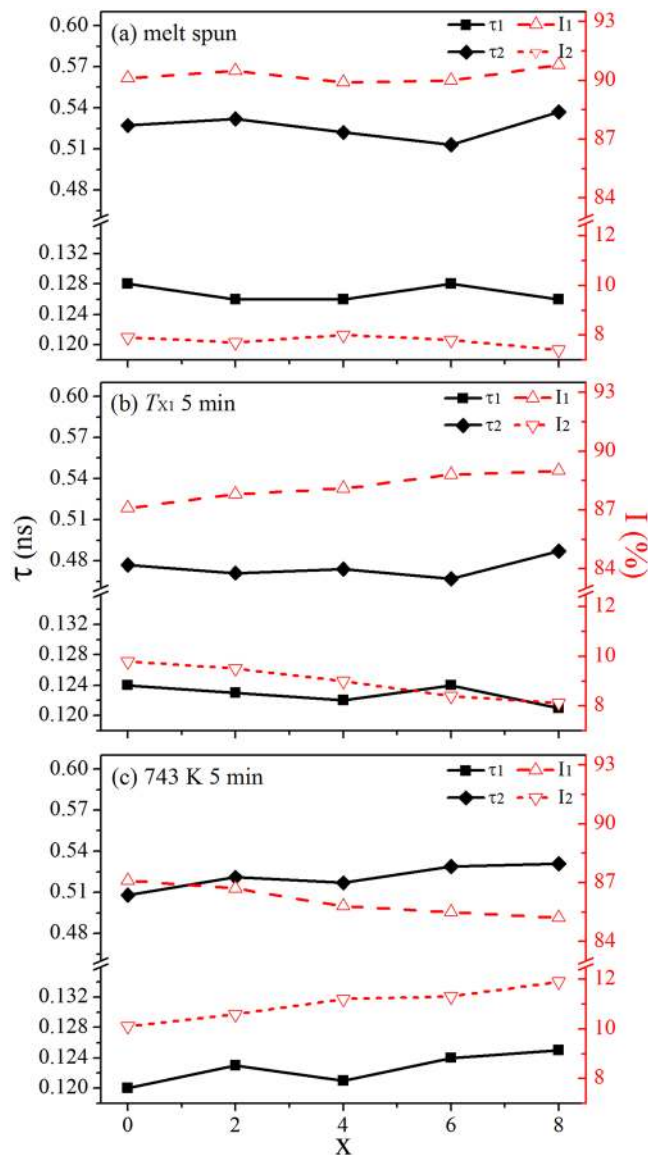
Figure 6. Positron lifetime components τ_1 and τ_2 with their respective intensity I_1 and I_2 of $Fe_{81}Si_xB_{10}P_{8-x}Cu_1$ ($x = 0{\sim}8$) melt spun ribbons (**a**) and those annealed at T_{X1} (**b**) and 743 K (**c**) for 5 min.

Structural defects and nucleation sites.   Structural defects of the $Fe_{81}Si_xB_{10}P_{8-x}Cu_1$ ($x = 0$, 2, 4, 6 and 8) alloys at various states are analyzed by PALS as shown in Fig. 6. Due to the formation of various free volume defects during the rapid solidification, positron lifetime spectra from all the samples can be best fitted to three lifetime components (τ_1, τ_2 and τ_3) representing three different vacancy defects whose respective intensities are defined as I_1, I_2 and I_3. The relative errors of all the components and their intensities remain in the limit of ± 0.5 %. The shortest lifetime τ_1 can be ascribed to the positron lifetime in interstitial holes in the polyhedral packing model which best describes several metallic glasses[36]. The intermediate lifetime τ_2 is related to the positron annihilation in nanovoids in the amorphous matrix and at grain boundaries formed during the annealing[37]. The longest lifetime τ_3 with values of more than 3 ns and intensities of less than 3 % is associated with the ortho-positronium annihilation occurring at the surface between the source and samples, as well as the internal surfaces between the ribbon sheets in the sandwiched samples[38], and thus it is not given here.

As shown in Fig. 6(a), for the melt spun alloy ribbons, τ_1 values of about 0.127 ns are shorter than 0.175 ns in the pure iron containing crystal mono-vacancy defects[20], while τ_2 values ranging from 0.513 ns to 0.537 ns indicate the free volume in nanovoids equivalent to at least five atom vacancy clusters in the amorphous structures[39]. A. P. Srivastava *et al.*[40] and L. Z. Lu *et al.*[41] have investigated the respective glass-forming ability of $Co_{69}Fe_xSi_{21-x}B_{10}$ and $Fe_{48-x}Co_xCr_{15}Mo_{14}C_{15}B_6Y_2$ amorphous alloys by comparing the conspicuous change in sizes of free volume and their intensities. However, τ_1, τ_2 and their corresponding intensities in Fig. 6(a) seem to have no significant fluctuation versus x, which implies that there exists no distinct difference in the glass-forming ability of the $Fe_{81}Si_xB_{10}P_{8-x}Cu_1$ amorphous alloys.

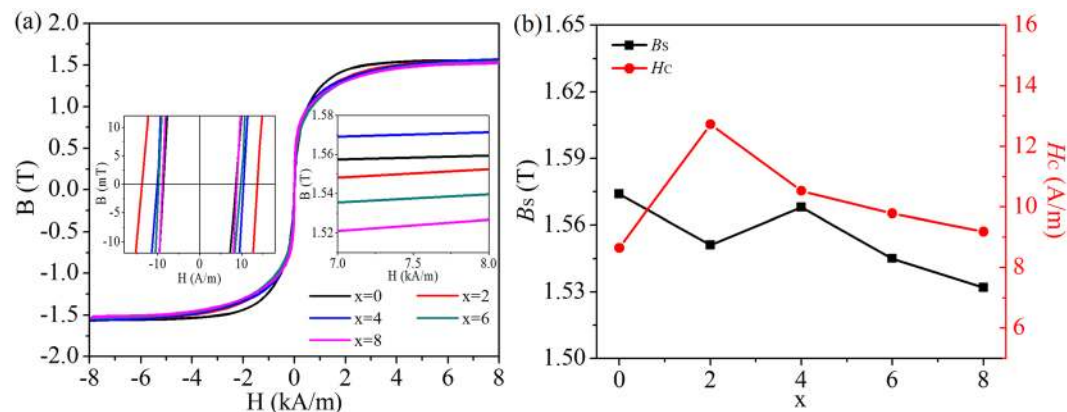**Figure 7.** *B-H* curves of melt spun $Fe_{81}Si_xB_{10}P_{8-x}Cu_1$ ($x=0\sim8$) ribbons with partially enlarged drawings inserted (**a**) and corresponding variation in B_S and H_C versus *x* (**b**).
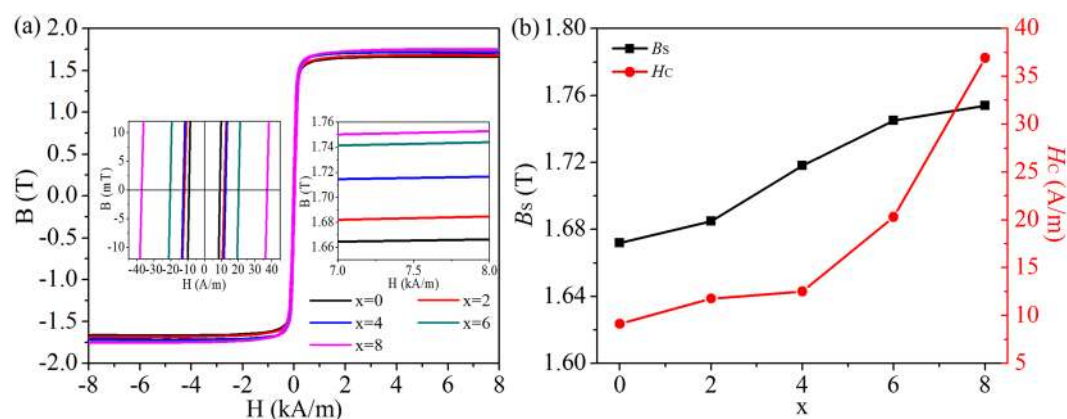

Figure 8. *B-H* curves of nanocrystalline $Fe_{81}Si_xB_{10}P_{8-x}Cu_1$ ($x=0\sim8$) ribbons with partially enlarged drawings inserted (**a**) and corresponding change in B_S and H_C versus *x* (**b**).

When $Fe_{81}Si_xB_{10}P_{8-x}Cu_1$ alloys are annealed at their primary crystallization temperature (T_{X1}) for 5 min, τ_1 and τ_2 values in Fig. 6(b) decrease slightly compared with those in Fig. 6(a), which means the defect sizes in the amorphous matrix reduce due to the structure compaction during the annealing. I_2 associated with the content of nanovoids increases drastically after the annealing, which can be attributed to the formation of numerous crystallites. Therefore, the obvious downward trend of I_2 in Fig. 6(b) illustrates that the content of crystallites at the beginning of crystallization declines with P gradual replaced by Si. It is reported that CuP clusters (Cu_3P like) separate from the amorphous matrix during the annealing and serve as the heterogeneous nucleation sites for crystallites in FeSiBPCu amorphous alloys[42]. More crystallites will precipitate out with more nucleation sites at the very beginning of crystallization, thus the trend of I_2 in Fig. 6(b) reflects the decrease in the density of heterogeneous nucleation sites in $Fe_{81}Si_xB_{10}P_{8-x}Cu_1$ alloys, which can be attributed to the reduction of beneficial CuP clusters in the amorphous matrix due to the amount of P decreasing.

Figure 6(c) shows τ_1, τ_2 and their corresponding intensities of the $Fe_{81}Si_xB_{10}P_{8-x}Cu_1$ nanocrystalline alloys. The value of τ_1 still has no obvious change after the crystallization, while τ_2 increases visually because of the grain growth. The upward trend of I_2 in Fig. 6(c) is ascribed to the increase of grain boundaries versus *x*, which suggests that the crystallinity increases with P replaced by Si in the $Fe_{81}Si_xB_{10}P_{8-x}Cu_1$ nanocrystalline alloys. It agrees well with the results of XRD and Mössbauer spectroscopy.

Magnetic properties. Figure 7 shows *B-H* loops and Si content dependence of B_S and H_C of the $Fe_{81}Si_xB_{10}P_{8-x}Cu_1$ ($x=0, 2, 4, 6$ and 8) melt spun alloys. It can be found that both $Fe_{81}B_{10}P_8Cu_1$ and $Fe_{81}Si_4B_{10}P_4Cu_1$ melt spun alloys exhibit relatively high B_S, which is consistent with the result of $B_{hf,a}$. On the other hand, H_C initially increases to a maximum in the $Fe_{81}Si_2B_{10}P_6Cu_1$ alloy and subsequently decreases, which can be attributed to the variation in magnetic anisotropy associated with the homogeneity of the amorphous matrix observed by Mössbauer spectra.

Figure 8 shows *B-H* loops as well as B_S and H_C versus Si content of the $Fe_{81}Si_xB_{10}P_{8-x}Cu_1$ ($x=0, 2, 4, 6$ and 8) nanocrystalline alloys. The value of B_S of nanocrystalline alloys can be calculated with the following formula[43]:

$$B_S = B_{SC}R + B_{SA}(1 - R)$$

where R is the crystallinity, B_{SC} and B_{SA} are the saturation magnetic flux densities of the crystalline and amorphous phases, respectively. Therefore, B_S strongly depends on the crystallinity R because B_{SC} is larger than B_{SA}. On Si substituting P, due to the replacement of Fe by nonmagnetic Si in bcc structure, the average magnetic moment of nanocrystallites inevitably decreases. However, the increase of crystallinity dominates with Si substituting for P in the $Fe_{81}Si_xB_{10}P_{8-x}Cu_1$ alloys, which results in the improvement of B_S from 1.67 T to 1.75 T. As $H_C \propto D^6$ (D is the average grain size)[44], the increase of H_C from 9.13 A/m to 36.92 A/m with x increasing can be attributed to the grain growth due to the inhibiting effect of P and CuP clusters on grain growth diminishing.

The $Fe_{81}Si_4B_{10}P_4Cu_1$ alloy, whether melt spun or nanocrystallized, exhibits simultaneously high B_S and low H_C compared with the others. It implies that the appropriate content ratio of Si and P in the $Fe_{81}Si_xB_{10}P_{8-x}Cu_1$ alloys can not only increase topological structure and homogenize the amorphous matrix, but also provide adequate heterogeneous nucleation sites and promote the crystallinity, all of which contribute to the enhancement of magnetic properties.

Conclusions

The microstructure of $Fe_{81}Si_xB_{10}P_{8-x}Cu_1$ ($x = 0, 2, 4, 6$ and 8) alloys and their crystallization mechanism are investigated by Mössbauer spectroscopy and positron annihilation technique. The topological structure and chemical homogeneity vary a lot even if the Fe content remains the same. Meanwhile, the reduction of crystallites at the early stage of crystallization suggests that the density of heterogeneous nucleation sites decreases with the increase of x during the annealing, which can reflect the variation in the content of beneficial CuP clusters in the amorphous matrix. Although the grains gradually coarsen with Si substituting for P, the inhibiting effect of CuP clusters and P atoms on the grain growth diminishes leading to the increase of crystallinity. Furthermore, Si tends to occupy lattice positions in bcc Fe, which results in the average magnetic moment of nanograins decreasing, but its contribution to B_S seems to be far less than that from the increase of the crystallinity. Tuning the content of Si and P appropriately in the FeSiBPCu alloys can not only improve the topological structure to strengthen the magnetic interaction in the amorphous matrix and the chemical homogeneity to decrease the magnetic anisotropy, but also optimizes effective CuP clusters during the crystallization to refine nanograins and finally promotes the crystallinity, which is an efficient method to improve synthetical magnetic properties without sacrificing the glass-forming ability.

Methods

The $Fe_{81}Si_xB_{10}P_{8-x}Cu_1$ ($x = 0, 2, 4, 6$ and 8) alloy ingots were prepared by induction melting mixtures of industrial raw materials Fe (99.90%), Cu (99.99%), Si-Fe (Si: 99.59%, Fe: 0.27%), P-Fe (P: 26.11%, Fe: 73.80%), B-Fe (B: 17%, Fe: 82.90%) in a Ti-deoxidant argon atmosphere. To ensure the homogeneity of chemical components, they were remelted four times with electromagnetic mixing. Amorphous ribbons with a cross section of about 0.02×2.5 mm^2 were then produced by a melt-spinning technique on a single-roller copper-wheel under argon atmosphere with a surface velocity of about 40 m/s. Thermal properties of melt-spun ribbons were measured by DSC at a heating rate of 20 K/min under high purity argon flow. To investigate the density of heterogeneous nucleation sites at the beginning of primary crystallization, the $Fe_{81}Si_xB_{10}P_{8-x}Cu_1$ ($x = 0, 2, 4, 6$ and 8) amorphous ribbons sandwiched by two quartz plates were sealed in a high vacuum furnace and isothermally annealed at their individual primary crystallization temperature T_{x1} obtained from DSC curves for 5 min by furnace cooling. Nanocrystalline ribbons were obtained by annealing the melt spun alloy ribbons at 743 K for 5 min. All the annealing is carried out with a heating rate of 1 K/s.

The microstructure of melt spun and annealed ribbons was characterized using both XRD with Cu Kα radiation ($\lambda = 0.154056$ nm) and room-temperature Mössbauer spectroscopy with ^{57}Co as γ-ray source. Velocity calibration of Mössbauer spectroscopy was accomplished by an α-Fe foil of 25 μm thickness. With assuming a distribution of hyperfine fields, Mössbauer spectra were analyzed by a least-square fitting procedure with NORMOS program[45]. TEM specimens were prepared adopting ion thinning at both sides of ribbons and then investigated by Tecnai 12 at 120 kV. PALS was employed to obtain detailed information about the free volume in melt spun and annealed ribbons. Specimens for PALS measurement were composed of two stacks of 10 layers of the sample ribbon with the ^{22}Na source sandwiched between them to ensure the annihilation of positrons within the volume of samples. Positron annihilation lifetime spectra had 10^6 counts and the time resolution of the spectrometer was 230 ps. Each positron lifetime was fitted in three components by using LT software version 9[46]. H_C and B_S of samples were measured by DC B-H loop tracer.

References

1. Lopatina, E. *et al*. Surface crystallization and magnetic properties of $Fe_{84.3}Cu_{0.7}Si_4B_8P_3$ soft magnetic ribbons. *Acta Mater.* **96**, 10–17 (2015).
2. Taghvaei, A. H. *et al*. Microstructure and magnetic properties of amorphous/nanocrystalline $Co_{40}Fe_{22}Ta_8B_{30}$ alloy produced by mechanical alloying. *Mater. Chem. Phys.* **134**, 1214–1224 (2012).
3. Herzer, G. Modern soft magnets: Amorphous, nanocrystalline materials. *Acta Mater.* **61**, 718–734 (2013).
4. Naz, G. J., Dong, D. D., Geng, Y. X., Wang, Y. M. & Dong, C. Composition formulas of Fe-based transition metals-metalloid bulk metallic glasses derived from dualcluster model of binary eutectics. *Sci. Rep.* **7**, 9150 (2017).
5. Yoshizawa, Y., Oguma, S. & Yamauchi, K. New Fe-based soft magnetic alloys composed of ultrafine grain structure. *J. Appl. Phys.* **64**, 6044–6046 (1988).
6. Makino, A. *et al*. Low core losses and magnetic properties of $Fe_{85-86}Si_{1-2}B_8P_4Cu_1$ nanocrystalline alloys with high B for power applications. *J. Appl. Phys.* **109**, 07A302 (2011).
7. Miglierini, M. *et al*. Magnetic microstructure of NANOPERM-type nanocrystalline alloys. *Phys. Status Solidi B* **243**, 57–64 (2006).
8. Lashgari, H. R. *et al*. Composition dependence of the microstructure and soft magnetic properties of Fe-based amorphous/nanocrystalline alloys: A review study. *J. Non Cryst. Solids* **391**, 61–82 (2014).

9. Ohta, M. & Yoshizawa, Y. Magnetic properties of nanocrystalline $Fe_{82.65}Cu_{1.35}Si_xB_{16-x}$ alloys ($x = 0$–7). *J. Appl. Phys.* **91**, 062517 (2007).

10. Hono, K., Ping, D. H., Ohnuma, M. & Onodera, H. Cu clustering and Si partitioning in the early crystallization stage of an $Fe_{73.5}Si_{13.5}B_9Nb_3Cu_1$ amorphous alloy. *Acta Mater.* **47**, 997–1006 (1999).

11. Ayers, J. D., Harris, V. G., Sprague, J. A., Elam, W. T. & Jones, H. N. *Acta Meter.* **46**, 1861–1874 (1998).

12. Makino, A., Men, H., Kubota, T., Yubuta, K. & Inoue, A. FeSiBPCu Nanocrystalline Soft Magnetic Alloys with High B_S of 1.9 Tesla Produced by Crystallizing Hetero-Amorphous Phase. *Mater. Trans.* **50**, 204–209 (2008).

13. Silveyra, J. M., Cremaschi, V. J., Janičkovič, D., Švec, P. & Arcondo, B. Structural and magnetic study of Mo-doped FINEMET. *J. Magn. Magn. Mater.* **323**, 290–296 (2011).

14. Parsons, R. *et al.* Effect of Si on the field-induced anisotropy in Fe-rich nanocrystalline soft magnetic alloys. *J. Alloy. Compd.* **695**, 3156–3162 (2017).

15. Srinivas, M., Majumdar, B., Bysakh, S., Raja, M. M. & Akhtar, D. Role of Si on structure and soft magnetic properties of $Fe_{87-x}Si_xB_9Nb_3Cu_1$ Ribbons. *J. Alloy. Compd.* **583**, 427–433 (2014).

16. Makino, A., Men, H., Kubota, T., Yubuta, K. & Inoue, A. New Fe-metalloids based nanocrystalline alloys with high B_S of 1.9T and excellent magnetic softness. *J. Appl. Phys.* **105**, 07A308 (2009).

17. Wu, Y. Q., Bitoh, T., Hono, K., Makino, A. & Inoue, A. Microstructure and properties of nanocrystalline Fe-Zr-Nb-B soft magnetic alloys with low magnetostriction. *Acta Mater.* **49**, 4069–4077 (2001).

18. Roy, R. K., Shen, S., Kernion, S. J. & McHenry, M. E. Effect of P addition on nanocrystallization and high temperature magnetic properties of low B and Nb containing FeCo nanocomposites. *J. Appl. Phys.* **111**, 07A301 (2012).

19. Sawatzki, S., Kübel, C., Ener, S. & Gutfleisch, O. Grain boundary diffusion in nanocrystalline Nd-Fe-B permanent magnets with low-melting eutectics. *Acta Mater.* **115**, 354–363 (2016).

20. Krištiaková, K. & Švec, P. Origin of cluster and void structure in melt-quenched Fe-Co-B metallic glasses determined by positron annihilation at low temperatures. *Phys. Rev. B* **64**, 014204 (2001).

21. Lashgari, H. R., Cadogan, J. M., Chu, D. & Li, S. The effect of heat treatment and cyclic loading on nanoindentation behaviour of FeSiB amorphous alloy. *Mater. Des.* **92**, 919–931 (2016).

22. Kohout, J. *et al.* Low temperature behavior of hyperfine fields in amorphous and nanocrystalline FeMoCuB. *J. Appl. Phys.* **117**, 17B718 (2015).

23. Babilas, R., Mariola, K. G., Burian, A. & Temleitner, L. A short-range ordering in soft magnetic Fe-based metallic glasses studied by Mössbauer spectroscopy and Reverse Monte Carlo method. *J. Magn. Magn. Mater.* **406**, 171–178 (2016).

24. Nabiałek, M. Influence of the Quenching Rate on the Structure and Magnetic Properties of the Fe-Based Amorphous Alloy. *Arch. Metall. Mater.* **61**, 439–444 (2016).

25. Torrens-Serra, J., Bruna, P., Roth, S., Rodriguez-Viejo, J. & Clavaguera-Mora, M. T. Structural and magnetic characterization of FeNbBCu alloys as a function of Nb content. *J. Phys. D: Appl. Phys.* **42**, 095010 (2009).

26. Cao, C. C. *et al.* Evolution of structural and magnetic properties of the FeCuBP amorphous alloy during annealing. *J. Alloy. Compd.* **722**, 394–399 (2017).

27. Cesnek, M. *et al.* Hyperfine interactions in nanocrystallized NANOPERM-type metallic glass containing Mo. *Hyperfine Interact.* **237**, 132 (2016).

28. Conde, C. F. *et al.* Magnetic and structural characterization of Mo-Hitperm alloys with different Fe/Co ratio. *J. Alloy. Compd.* **509**, 1994–2000 (2011).

29. Borrego, J. M. *et al.* Crystallization behavior and magnetic properties of Cu-containing Fe-Cr-Mo-Ga-P-C-B alloys. *J. Appl. Phys.* **100**, 043515 (2006).

30. Jiraskova, Y., Zabransky, K., Vujtek, M. & Zivotsky, O. Changes in the hyperfine interactions in the $Fe_{80}Nb_3Cu_1B_{16}$ metallic glass under tensile loading. *J. Magn. Magn. Mater.* **322**, 1939–1946 (2010).

31. Xia, G. T., Wang, Y. G., Dai, J. & Dai, Y. D. Effects of Cu cluster evolution on soft magnetic properties of $Fe_{83}B_{10}C_6Cu_1$ metallic glass in two-step annealing. *J. Alloys Compd.* **690**, 281–286 (2017).

32. Stearns, M. B. Internal Magnetic Fields, Isomer Shifts, and Relative Abundances of the Various Fe Sites in FeSi Alloys. *Phys. Rev. B* **129**, 1136–1144 (1963).

33. Pulido, E., Navarro, I. & Hernando, A. Mössbauer spectroscopy in nanocrystalline materials. *IEEE Trans. Magn.* **28**, 2424–2426 (1992).

34. Matsuura, M., Zhang, Y., Nishijima, M. & Makino, A. Role of P in Nanocrystallization of $Fe_{85}Si_2B_8P_4Cu_1$. *IEEE Trans. Magn.* **50**, 1–4 (2014).

35. Wang, Y. C., Takeuchi, A., Makino, A., Liang, Y. Y. & Kawazoe, Y. Nano-crystallization and magnetic mechanisms of $Fe_{85}Si_2B_8P_4Cu_1$ amorphous alloy by ab initio molecular dynamics simulation. *J. Appl. Phys.* **115**, 173910 (2014).

36. Gaskell, P. H. A new structural model for transition metal-metalloid glasses. *Nature.* **276**, 484–485 (1978).

37. Filipecka, K., Pawlik, P. & Filipecki, J. The effect of annealing on magnetic properties, phase structure and evolution of free volumes in Pr-Fe-B-W metallic glasses. *J. Alloy. Compd.* **694**, 228–234 (2017).

38. Tong, H. Y. *et al.* Investigations on nanocrystalline $Fe_{78}B_{13}Si_9$ alloys by positron annihilation spectroscopy. *J. Appl. Phys.* **72**, 5124–5129 (1992).

39. Srivastava, A. P. *et al.* Correlation of soft magnetic properties with free volume and medium range ordering in metallic glasses probed by fluctuation microscopy and positron annihilation technique. *J. Magn. Magn. Mater.* **324**, 2476–2482 (2012).

40. Srivastava, A. P. *et al.* Investigation of medium range order and glass forming ability of metallic glass $Co_{69}Fe_xSi_{21-x}B_{10}$ $x = 3$, 5, and 7. *J. Phys. D: Appl.Phys.* **49**, 225303 (2016).

41. Lu, Y. Z., Huang, Y. J., Zheng, W. & Shen, J. Free volume and viscosity of Fe-Co-Cr-Mo-C-B-Y bulk metallic glasses and their correlation with glass-forming ability. *J. Non Cryst. Solids* **358**, 1274–1277 (2012).

42. Makino, A. Nanocrystalline soft magnetic Fe-Si-B-P-Cu alloys with high *B* of 1.8–1.9 T contributable to energy saving. *IEEE Trans. Magn.* **48**, 1331–1335 (2012).

43. Ohata, M. & Yoshizawa, Y. Cu addition effect on soft magnetic properties in Fe-Si-B alloy system. *J. Appl. Phys.* **103**, 07E722 (2008).

44. Herzer, G. Grain size dependence of coercivity and permeability in nanocrystalline ferromagnets. *IEEE Trans. Magn.* **26**, 1397–1402 (1990).

45. Brand, R. A. Improving the validity of hyperfine field distributions from magnetic alloys: Part I: Unpolarized source. *Nucl. Instrum. Meth. B* **28**, 398–416 (1987).

46. Kansy, J. Microcomputer program for analysis of positron annihilation lifetime spectra. *Nucl. Instrum. Meth. A* **374**, 235–244 (1996).

Acknowledgements

Author Contributions

C.C.C. conceived and designed the research. Y.D.D., F.M.P. and J.K.C. gave guidance for experiments. C.C.C., L.Z., Y.M. and X.B.Z. wrote the manuscript. Y.G.W. commented on the manuscript writing and the result discussions. All authors discussed the results and revised the manuscript.

Additional Information

Competing Interests: The authors declare that they have no competing interests.

Publisher's note: Springer Nature remains neutral with regard to jurisdictional claims in published maps and institutional affiliations.